

LETTER • OPEN ACCESS

# High-power and efficiency W-band InAlGa<sub>N</sub>/AlN/GaN high-electron-mobility transistors for future high-capacity wireless communications

To cite this article: Yusuke Kumazaki *et al* 2024 *Appl. Phys. Express* **17** 086504

View the [article online](#) for updates and enhancements.

## You may also like

- [Experimental and simulation study on ultraviolet light emission from quaternary InAlGa<sub>N</sub> quantum wells with localized carriers](#)  
Makoto Miyoshi, Masataka Kato and Takashi Egawa
- [Probing the effects of surface roughness and barrier layer thickness in InAlGa<sub>N</sub>/Ga<sub>N</sub> HEMTs to improve carrier mobility](#)  
Junya Yaita, Atsuthi Yamada, Norikazu Nakamura *et al.*
- [Enhancement-Mode High-Frequency InAlGa<sub>N</sub>/Ga<sub>N</sub> MIS-HEMT Fabricated by Implementing Oxygen-Based Digital Etching on the Quaternary Layer](#)  
Ping-Yu Tsai, Hoang-Tan-Ngoc Nguyen, Venkatesan Nagarajan *et al.*



## High-power and efficiency W-band InAlGaN/AlN/GaN high-electron-mobility transistors for future high-capacity wireless communications

Yusuke Kumazaki\*, Shiro Ozaki, Yasuhiro Nakasha, Naoya Okamoto, Atsushi Yamada , and Toshihiro Ohki

Fujitsu Limited, Kawasaki, Kanagawa, 211-8588, Japan

\*E-mail: [kumazaki.yusuke@fujitsu.com](mailto:kumazaki.yusuke@fujitsu.com)

Received June 15, 2024; revised July 14, 2024; accepted July 29, 2024; published online August 26, 2024

This study describes high-power and high-efficiency W-band InAlGaN/AlN/GaN high-electron-mobility transistors (HEMTs) for future sub-terahertz wireless communications. A low-thermal-budget selective-area growth (SAG) process was developed to obtain low contact resistance with low trap states. Transmission lines and substrate structures were optimized to obtain high-thermal conductivity and low substrate resonance. Consequently, a high output power of 28.7 dBm (742 mW), output power density of 4.6 W mm<sup>-1</sup>, and power-added efficiency (PAE) of 28.0% were achieved with pre-matched InAlGaN/AlN/GaN HEMTs at 90 GHz, which were superior combination of output power and PAE compared to the conventional high-temperature SAG process. © 2024 The Author(s). Published on behalf of The Japan Society of Applied Physics by IOP Publishing Ltd

The rapid spread of smartphones and Internet-of-things devices has led to an ever-increasing data traffic.<sup>1)</sup> Expected use cases, i.e. extended reality, wireless robotics, fully autonomous vehicles/robotics, and telepresence, will demand extremely low latency, ultra-high reliability, and data rates for future wireless communications.<sup>2–4)</sup> Although the sub-6 GHz and millimeter-wave bands are specified as 5 G new radio (NR),<sup>5)</sup> the requirements of above use cases have not yet been met partially because of the limited bandwidth and number of channels. A sub-terahertz range (90–300 GHz) is abundant in unoccupied frequency resources and thereby can provide enormous network capacity.<sup>6)</sup> The 100 GHz band (e.g. 92–100 and 102–109.5 GHz, allocated for land mobiles and fixed wireless access by the International Telecommunication Union Radiocommunication Sector<sup>7)</sup>) is one of the expected frequency bands utilized for future wireless communication because their features include wider bandwidth than each of 5 G NR frequency bands<sup>8)</sup> and less atmospheric attenuation than upper sub-terahertz bands.<sup>9)</sup> However, compared with sub-6 GHz and millimeter-wave band PAs, the 100 GHz band is hindered by limited power amplifier (PA) performance.<sup>10)</sup> GaN-based high-electron-mobility transistors (HEMTs) are promising for their high-performance 100 GHz band PAs because they can realize high-voltage/high-current operations and high-frequency signal amplification simultaneously.<sup>11–13)</sup> Our group previously presented a high output power density of 3.6 W mm<sup>-1</sup> at 86 GHz by InAlGaN/AlN/GaN HEMTs and 4.6 W mm<sup>-1</sup> at 94 GHz by integrating a selective-area growth (SAG) ohmic contact and an InGaN back barrier;<sup>14,15)</sup> however, power-added efficiency (PAE) was below 15%, which must be improved for practical use. The PAE  $\eta_{\text{add}}$  with a class A operation can be expressed as follows:<sup>16)</sup>

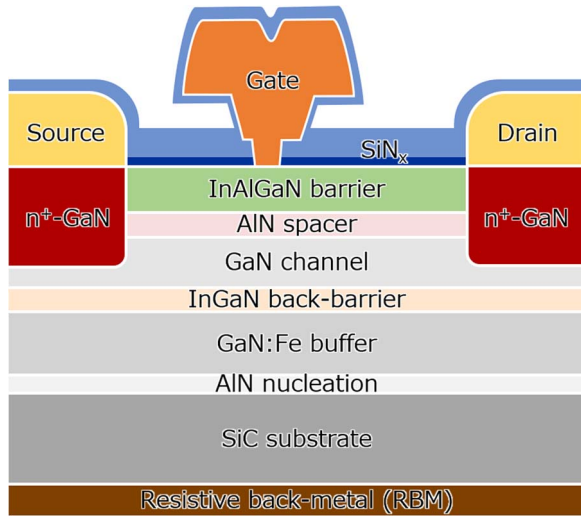
$$\eta_{\text{add}} = \eta_{\text{D}} \left( 1 - \frac{1}{G_{\text{P}}} \right) = \frac{1}{2} \left( 1 - \frac{V_{\text{min}}}{V_{\text{DS}}} \right) \left( 1 - \frac{1}{G_{\text{P}}} \right), \quad (1)$$

where  $\eta_{\text{D}}$  is the drain efficiency;  $G_{\text{P}}$  is the power gain,  $V_{\text{DS}}$  is the DC drain voltage, and  $V_{\text{min}}$  is the instantaneous minimum drain voltage under radiofrequency operation. The PAE can be affected by  $V_{\text{min}}/V_{\text{ds}}$  and power gain, and they are deteriorated by trap-related transient behavior, called current collapse. We confirmed that a high-temperature (HT) SAG process induced trap states and enhanced current collapse.<sup>17)</sup>

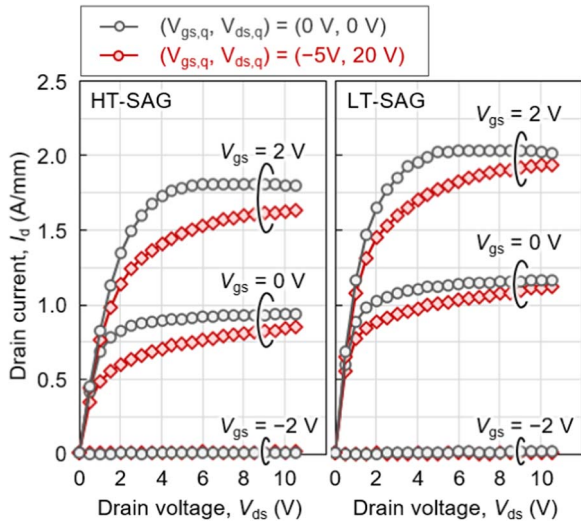
In the present study, high-power and high-efficiency W-band InAlGaN/AlN/GaN HEMTs with a low-thermal-budget (LT) SAG process were developed. The substrate structure was also optimized in terms of thermal management and propagation properties.

Figure 1 shows a schematic cross-section of InAlGaN/AlN/GaN HEMTs. The epitaxial structure was composed of one layer each of AlN nucleation, Fe-doped GaN buffer, InGaN back barrier, GaN channel, AlN spacer, and InAlGaN barrier, which were grown on a SiC substrate by metalorganic vapor phase epitaxy (MOVPE). The typical sheet resistance  $R_{\text{sh}}$ , carrier density  $n_{\text{s}}$ , and mobility  $\mu$  of epitaxial structures were 250  $\Omega$  sq<sup>-1</sup>,  $1.2 \times 10^{13}$  cm<sup>-2</sup>, and 2080 cm<sup>2</sup> V<sup>-1</sup> s<sup>-1</sup>, respectively. Device fabrication was initiated via electrical isolation of elements through ion implantation. Subsequently, a SiN<sub>x</sub> surface-protection layer was formed by plasma-enhanced chemical vapor deposition (PECVD), which acts as a mask for the subsequent SAG process. A part of SiN<sub>x</sub> mask and InAlGaN/AlN/GaN layers were removed through inductively coupled plasma reactive ion etching (ICP-RIE), and the n<sup>+</sup>-GaN was grown by MOVPE. In a previous study,<sup>15)</sup> the SiN<sub>x</sub> mask should be removed by wet chemical etching after the SAG process because a polycrystalline GaN was formed on a mask and the SiN<sub>x</sub> became defective after the SAG process because of the HT growth condition ( $\sim 750$  °C). In this study, the pattern layout and growth conditions were optimized for the LT-SAG process ( $\sim 630$  °C) without polycrystalline growth on the mask. Then, the Ti/Al metals were evaporated, and post-metallization annealing was conducted at 600 °C for 1 min, thus affording the source/drain electrodes with a typical contact resistance of 0.1  $\Omega$ ·mm. After the Ohmic contact formation, the second passivation layer was formed by PECVD. The gate footprint was defined by electron beam lithography, and the exposed SiN was removed through ICP-RIE. The Ni/Au-based gate electrode was formed through evaporation and a lift-off process using the trilayer resist technique. The gate length  $L_{\text{g}}$ , the source–gate spacing  $L_{\text{sg}}$ , and the gate–drain spacing  $L_{\text{gd}}$  were 0.08, 0.5, and 0.8  $\mu$ m, respectively. Figure 2 shows the pulsed  $I_{\text{d}}-V_{\text{ds}}$  characteristics of InAlGaN/AlN/GaN HEMTs with HT-SAG and LT-SAG processes. The quiescent gate and drain voltages ( $V_{\text{gs,q}}$ ,  $V_{\text{ds,q}}$ ) were (0 V, 0 V) and (–5 V, 20 V), respectively. The pulse





**Fig. 1.** Cross-sectional diagram of InAlGaN/AlN/GaN HEMTs with a selective-area growth (SAG) ohmic contact and a resistive back metal (RBM).



**Fig. 2.** Pulsed  $I_d$ - $V_{ds}$  characteristics of InAlGaN/AlN/GaN HEMTs with high-temperature (HT) and low-temperature (LT) SAG processes.

width was  $1\ \mu\text{s}$  and a duty cycle was 0.1%. The HT-SAG device showed a maximum drain current  $I_{d,\text{max}}$  of  $1.78\ \text{A mm}^{-1}$  and on-resistance  $R_{\text{ON}}$  of  $1.35\ \Omega\cdot\text{mm}$  under non-stressed conditions, and the knee current  $I_k$  was reduced by 17.5% under stressed conditions. The LT-SAG device showed improved  $I_{d,\text{max}}$  of  $2.01\ \text{A mm}^{-1}$ , on-resistance  $R_{\text{ON}}$  of  $1.03\ \Omega\cdot\text{mm}$ , and  $I_k$ -reduction of 12.5%. According to Van der Paul method, the  $\mu$  and  $n_s$  were  $1570\ \text{cm}^2\text{V}^{-1}\text{s}^{-1}$  and  $1.4 \times 10^{13}\ \text{cm}^{-2}$  for HT-SAG devices, whereas those were  $1950\ \text{cm}^2\text{V}^{-1}\text{s}^{-1}$  and  $1.4 \times 10^{13}\ \text{cm}^{-2}$  for LT-SAG devices. As-deposited  $\text{SiN}_x$  used as the first passivation layer in HT-SAG devices included the amount of hydrogen impurities caused by insufficient ionization of monosilane. Fourier-transform infrared spectroscopy revealed that hydrogen bonds accounted for approximately 35% of Si-N bonds in as-deposited  $\text{SiN}_x$  and reduced to below 10% in  $\text{SiN}_x$  sintered at  $600^\circ\text{C}$ , which nearly corresponded to the thermal budget of the LT-SAG process. A study reported that hydrogen atoms at nitrogen vacancy were responsible for electron localization,<sup>18)</sup> which could cause potential fluctuations and reduce electron

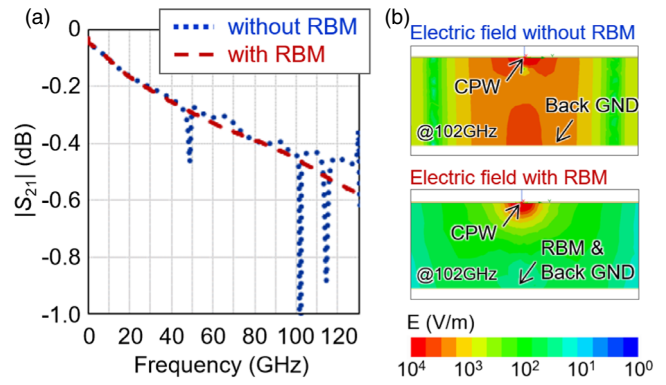


**Fig. 3.** (a) Simulated propagation losses and (b) electric field in the substrate of  $50\ \Omega$  coplanar waveguides with and without RBM.

mobility by remote Coulomb scattering.<sup>19)</sup> In addition, the HT-SAG process includes the removal of the  $\text{SiN}_x$  mask and additional  $\text{SiN}_x$  deposition on the semiconductor surface by PECVD, which could induce damage at the interface between the  $\text{SiN}_x$  and the InAlGaN barrier layer. We believe that the improvement of pulsed  $I_d$ - $V_{ds}$  characteristics obtained with the LT-SAG process originated from the reduction of the trap states in the  $\text{SiN}_x$  film and interface.

A backside process comprises grinding and polishing of the SiC substrate, metallization, and dicing. Generally, the substrate is thinned to  $50$ – $100\ \mu\text{m}$  to obtain a characteristic impedance of  $50\ \Omega$  in microstrip transmission lines with comparable dimensions to transistors. On the contrary, thinning the SiC substrates leads to the degradation of heat transfer confirmed by a computational fluid dynamics solver.<sup>20)</sup> We employed  $350\ \mu\text{m}$  thick SiC substrates and a coplanar waveguide (CPW) whose characteristic impedance did not correlate with the substrate's thickness. Substrate resonance is another issue because the wavelength of a  $100\ \text{GHz}$  wave is close to the substrate thickness. We employed  $100\ \text{nm}$  thick Ni-Cr film as a resistive back metal (RBM) (Fig. 1) to attenuate the propagated signal. Figure 3(a) shows the transmission properties of  $50\ \Omega$  CPWs with a length of  $1\ \text{mm}$  calculated by electromagnetic-field simulation software. The CPW without RBM showed destructive interference because of substrate resonance, particularly at high frequency [Fig. 3(b)]. The CPW with RBM showed straightforward characteristics reflecting dielectric loss, indicating that an RBM is effective in suppressing the substrate resonance.

We designed pre-matching circuits as shown in Fig. 4(a) to evaluate the power performance of InAlGaN/AlN/GaN HEMTs. The gate periphery  $W_g$  of the transistor was  $0.16\ \text{mm}$  ( $4 \times 40\ \mu\text{m}$ ). The cut-off frequency  $f_T$  and maximum oscillation frequency  $f_{\text{max}}$  were estimated as  $89$  and  $310\ \text{GHz}$ , respectively. The reflection coefficient of source  $\Gamma_S$  and load  $\Gamma_L$  of transistors were  $0.71$  and  $0.43$  at  $90\ \text{GHz}$ , respectively. Because the  $\Gamma_S$  was too high to adjust the impedance precisely with our load-pull system, the input matching network was designed to transform the source impedance of transistor to approximately  $50\ \Omega$ . As for the output matching network, no passive components, except for short  $50\text{-}\Omega$  transmission lines, were embedded because the  $\Gamma_L$  of the transistor was in the adjustable range of equipment. The MAG values of the input and output matching networks

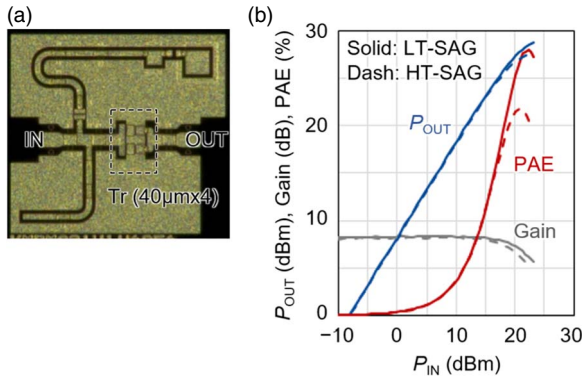


**Fig. 4.** (a) Micrograph and (b) large-signal characteristics of pre-matched InAlGaN/AlN/GaN HEMTs.

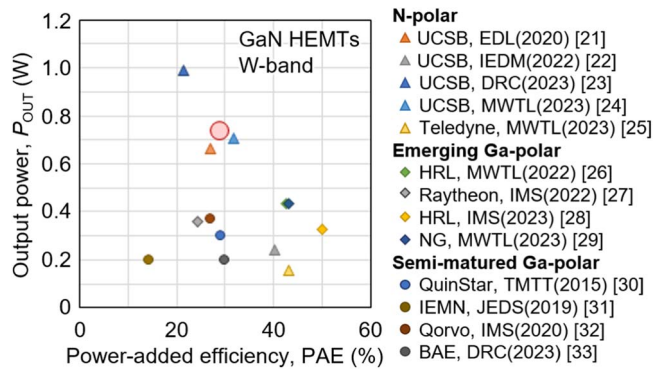


**Fig. 5.** Comparison of the load-pull power performance of W-band GaN HEMTs.

were  $-0.47$  and  $-0.02$  dB at 90 GHz, respectively, which was used for de-embedding the circuit loss and extracting the transistor power performance. Figure 4(b) shows the input–output power ( $P_{IN}$ – $P_{OUT}$ ) characteristics of pre-matched InAlGaN/AlN/GaN HEMTs at 90 GHz. The transistors were biased at the  $V_{gs}$  of  $-1.2$  V and  $V_{ds}$  of 20 V. The saturated  $P_{OUT}$ , power density, and PAE were 27.5 dBm (566 mW),  $3.5$  W mm $^{-1}$ , and 21.8% with HT-SAG devices and 28.7 dBm (742 mW),  $4.6$  W mm $^{-1}$ , and 28.0% with LT-SAG devices, respectively. Compared with our previous work,<sup>14,15</sup> we obtained a good combination of power density and PAE, which was mostly attributed to the suppression of the current collapse and increase of power gain by the LT-SAG process and optimized substrate structures. Figure 5 summarizes the current state-of-the-art W-band GaN HEMTs.<sup>21–33</sup> Our InAlGaN/AlN/GaN HEMTs demonstrated the highest output power among the semi-matured Ga-polar HEMTs, and good power performance enough to compete with emerging Ga-polar and N-polar devices.

In summary, high-performance W-band InAlGaN/AlN/GaN HEMTs were demonstrated. DC characteristics were enhanced by the LT-SAG process, which is likely caused by the reduction of defects in the SiN $_x$  film and interface. The CPWs with RBM were employed for transmission lines to obtain high-thermal conductivity with thick SiC substrates and suppress unwanted signal propagation in the substrates. Consequently, our InAlGaN/AlN/GaN HEMTs demonstrated higher PAE than our previous devices and the highest output power among the semi-matured Ga-polar HEMTs at W-band,

indicating that these technologies are beneficial for future sub-terahertz wireless communications.

**Acknowledgments** This work was partially supported by “The research and development project for the expansion of radio spectrum resources (JPJ000254)” of the Ministry of Internal Affairs and Communication, Japan. The authors would like to thank Takayuki Fujiwara, Atsushi Takahashi, Yasuyuki Ishii, and Naoki Okada for their support in device fabrication and characterization.

**ORCID iDs** Atsushi Yamada <https://orcid.org/0000-0002-3317-2365>

- Ericsson, Mobile data traffic outlook, <https://ericsson.com/en/reports-and-papers/mobility-report/dataforecasts/mobile-traffic-forecast> (2022).
- J. Wallace and A. Valdivia, Int. Conf. on Computational Science and Computational Intelligence (CSCI) (Las Vegas, NV, USA), 2021, p. 1291, 10.1109/CSCI54926.2021.00264.
- L. Qiao, Y. Li, D. Chen, S. Serikawa, M. Guizani, and Z. Lv, *Comput. Electr. Eng.* **95**, 107372 (2021).
- M. Z. Chowdhury, M. Shahjalal, S. Ahmed, and Y. M. Jang, *IEEE Open J. Commun. Soc.* **1**, 957 (2020).
- S. Parkvall, E. Dahlman, A. Furuskar, and M. Frenne, *IEEE Commun. Standards Mag.* **1**, 24 (2017).
- S. Bicaïs, J.-B. Doré, G. Gougéon, and Y. Corre, *IEEE Int. Conf. Acoust., Speech Signal Process. (ICASSP)* (Barcelona, Spain), 2020, p. 5095, 10.1109/ICASSP40776.2020.9052917.
- ITU-R, Report ITU-R M.2500-0, 2021, (<https://itu.int/pub/R-REP-M.2500>).
- N.-N. Dao, N. H. Tu, T.-D. Hoang, T.-H. Nguyen, L. V. Nguyen, K. Lee, L. Park, W. Na, and S. Cho, *Comput. Netw.* **245**, 110370 (2024).
- ITU-R, Recommendation ITU-R P.676-13, 2022, <https://www.itu.int/rec/R-REC-P.676-13-202208-I/en>.
- V. Camarchia, R. Quaglia, A. Piacibello, D. P. Nguyen, H. Wang, and A.-V. Pham, *IEEE Trans. Microw. Theory Techn.* **68**, 2957 (2020).
- D. S. Lee, Z. Liu, and T. Palacios, *Jpn. J. Appl. Phys.* **53**, 100212 (2014).
- Y. Kumazaki et al., *Appl. Phys. Express* **14**, 016502 (2020).
- S. Ozaki, J. Yaita, A. Yamada, Y. Kumazaki, Y. Minoura, T. Ohki, N. Okamoto, N. Nakamura, and J. Kotani, *Appl. Phys. Express* **14**, 041004 (2021).
- Y. Niida et al., *IEEE Topical Conf. Power Modeling Wireless Radio Appl. (PAWR)* (Austin, TX, USA), 2016, p. 24, 10.1109/PAWR.2016.7440153.
- J. Kotani, K. Makiyama, T. Ohki, S. Ozaki, N. Okamoto, Y. Minoura, M. Sato, N. Nakamura, and Y. Miyamoto, *Electron. Lett.* **59**, 1 (2023).
- Y. Takayama, *IEICE Trans. Electron.* **E80-C**, 726733 (1997), ([https://search.ieice.org/bin/summary.php?id=e80-c\\_6\\_726](https://search.ieice.org/bin/summary.php?id=e80-c_6_726)).
- Y. Kumazaki, S. Ozaki, N. Okamoto, N. Hara, and T. Ohki, *IEEE Trans. Electron Devices* **69**, 3073 (2022).
- L.-S. Wang, J.-P. Xu, L. Liu, Y. Huang, H.-H. Lu, P.-T. Lai, and W.-M. Tang, *IEEE Trans. Nanotechnol.* **14**, 854 (2015).
- V. A. Gritsenko, S. S. Nekrashevich, V. V. Vasilev, and A. V. Shaposhnikov, *Microelectron. Eng.* **86**, 1866 (2009).
- N. Okamoto et al., Int. Conf. Compound Semiconductor Manuf. Technol. (CS-MANTECH) 2019, p. 10.5 ([https://csmantech.org/wp-content/acfireduploads/field\\_5e8cddf5ddd10/post\\_1317/010.5\\_S10\\_P5\\_OKAMOTO.pdf](https://csmantech.org/wp-content/acfireduploads/field_5e8cddf5ddd10/post_1317/010.5_S10_P5_OKAMOTO.pdf)).
- B. Romanczyk, X. Zheng, M. Guidry, H. Li, N. Hatui, C. Wurm, A. Krishna, E. Ahmadi, S. Keller, and U. K. Mishra, *IEEE Electron Device Lett.* **41**, 349 (2020).
- W. Li et al., Int. Electron Devices Meeting (IEDM) (San Francisco, CA, USA), 2022, p. 11.2.1, 10.1109/IEDM45625.2022.10019475.
- E. Akso et al., 2023 Device Research Conf. (DRC) (Santa Barbara, CA, USA), 2023, p. 1, 10.1109/DRC58590.2023.10187008.
- E. Akso et al., *IEEE Microw. Wireless Technol. Lett.* **33**, 683 (2023).
- A. Arias-Purdue et al., *IEEE Microw. Wireless Technol. Lett.* **33**, 1011 (2023).
- J.-S. Moon et al., *IEEE Microw. Wireless Compon. Lett.* **33**, 161 (2023).
- E. M. Chumbes, J. Logan, B. Schultz, M. DeJarlid, M. Tahhan, N. Kolias, M. Hardy, M. Ancona, and D. Meyer, *IEEE/MTT-S Int. Microwave Symp. (IMS)* (Denver, CO, USA), 2022, p. 295, 10.1109/IMS37962.2022.9865268.
- J.-S. Moon et al., *IEEE/MTT-S Int. Microwave Symp. (IMS)* (San Diego, CA, USA), 2023, p. 97, 10.1109/IMS37964.2023.10188089.
- R. S. Howell, B. Novak, T. Vassen, P. Shea, J. Chang, and S. Afroz, *IEEE Microw. Wireless Technol. Lett.* **33**, 839 (2023).
- J. M. Schellenberg, *IEEE Trans. Microw. Theory Techn.* **63**, 2833 (2015).
- K. Harrouche, R. Kabouche, E. Okada, and F. Medjdoub, *IEEE J. Electron Devices Soc.* **7**, 1145 (2019).
- Y. Cao et al., *IEEE/MTT-S Int. Microwave Symp. (IMS)* (Los Angeles, CA, USA), 2020, p. 570, 10.1109/IMS30576.2020.9223913.
- P. Srivastava et al., *Device Research Conf. (DRC)* (Santa Barbara, CA, USA), 2023, p. 1, 10.1109/DRC58590.2023.10186972.

© 2024 The Author(s). Published on behalf of